



Experimental and theoretical study of dense YBO₃ and the influence of non-hydrostaticity

Robin Turnbull ^{a,*}, Daniel Errandonea ^a, Vanesa Paula Cuenca-Gotor ^b, Juan Ángel Sans ^b, Oscar Gomis ^c, Alfonso Gonzalez ^d, Plácida Rodríguez-Hernandez ^d, Catalin Popescu ^e, Marco Bettinelli ^f, Karuna K. Mishra ^g, Francisco Javier Manjón ^b

^a Departamento de Física Aplicada - Instituto de Ciencia de Materiales, Matter at High Pressure (MALTA) Consolider Team, Universidad de Valencia, Edificio de Investigación, C/Dr. Moliner 50, Burjassot, 46100, Valencia, Spain

^b Instituto de Diseño para la Fabricación y Producción Automatizada, MALTA Consolider Team, Universitat Politècnica de València, Camí de Vera s/n, 46022, Valencia, Spain

^c Centro de Tecnologías Físicas, MALTA Consolider Team, Universitat Politècnica de València, 46022, Valencia, Spain

^d Departamento de Física Fundamental II, Instituto de Materiales y Nanotecnología, MALTA Consolider Team, Universidad de La Laguna, 38205, Tenerife, Spain

^e CELLS-ALBA Synchrotron Light Facility, 08290, Cerdanyola del Vallès, Barcelona, Spain

^f Luminescent Materials Laboratory, Department of Biotechnology, Università di Verona, and INSTM - University of Verona Research Unit, Strada Le Grazie 15, 37134, Verona, Italy

^g Department of Physics and Institute for Functional Nanomaterials, P.O. Box 70377, University of Puerto Rico, San Juan, PR 00936-8377, USA

ARTICLE INFO

Article history:

Received 24 April 2020

Received in revised form

25 June 2020

Accepted 27 July 2020

Available online 17 August 2020

Keywords:

High-pressure

Synchrotron radiation

X-ray diffraction

Inelastic light scattering

Phosphors

Anisotropy

ABSTRACT

YBO₃ is used in photonics applications as a host for red phosphors due to its desirable chemical stability, high quantum efficiency and luminescence intensity. Despite its fundamental thermodynamic nature, the isothermal bulk modulus of YBO₃ has remained a contentious issue due to a lack of comprehensive experimental and theoretical data and its vibrational modes are far from being understood. Here, we present an experimental-theoretical structural and vibrational study of YBO₃. From structural data obtained from synchrotron X-ray diffraction data and *ab initio* calculations, we have determined the YBO₃ bulk modulus, isothermal compressibility tensor and pressure-volume (*P-V*) equation of state (*EoS*). The isothermal compressibility tensor reveals that the compressibility of YBO₃ is highly anisotropic, with the principal compression axis lying perpendicular to the *ab*-plane being approximately twice as stiff as the two axes perpendicular to it. From the vibrational data obtained from Raman scattering measurements and *ab initio* calculations, the experimental and calculated pressure response of the YBO₃ Raman modes is also determined with the corresponding Grüneisen parameters and the symmetry of the experimental modes has been tentatively assigned and discussed. No evidence for a pressure-induced phase transition in YBO₃ is observed up to 27 GPa, however we note that an apparent discontinuity in the compressibility at 8 GPa, likely due to the onset of non-hydrostaticity, could lead to the misinterpretation of an atypically high bulk modulus.

© 2020 Elsevier B.V. All rights reserved.

1. Introduction

YBO₃ is an ideal host lattice for luminescent lanthanide ions (Eu³⁺, Tb³⁺, Ce³⁺) because it exhibits an exceptional optical damage threshold and high chemical stability. The chromaticity and luminescence intensity of YBO₃ can be tuned via the control parameters

of sample morphology, crystal size and relative doping concentrations of the activator ions [1–6]. Pressure offers a convenient thermodynamic route to control the structure and emergent photoluminescent properties of YBO₃ [7]. However, for YBO₃ even the fundamental parameter of the isothermal bulk modulus, $B = -V\partial P/\partial V$, has been the subject of debate. The exceptional high value of the experimental YBO₃ bulk modulus alleged in Ref. [8] ($B = 329 \pm 31$ GPa) received close criticism, with Ref. [9] providing *ab initio* calculations to support their critique that such behaviour in YBO₃ would contradict the known compressibility systematics of

* Corresponding author.

E-mail address: Robin_Turnbull@uv.es (R. Turnbull).

isomorphous borates [10] and that a much lower bulk modulus is predicted by theory ($B = 141$ GPa). Therefore, further experimental and theoretical data are required to illuminate the fundamental structural properties of YBO_3 . Additionally, although the vibrational properties of YBO_3 have been explored by Raman scattering (RS) at high pressure [7], the symmetry assignment of the observed Raman-active modes, and the discussion of their pressure dependence, has not been previously addressed.

Here, we present a comprehensive experimental-theoretical study of YBO_3 under isothermal compression up to 27 GPa. In particular, we determine the experimental isothermal compressibility tensor, pressure-volume (P - V) equation of state (EoS) and bulk modulus of YBO_3 from high-pressure synchrotron X-ray diffraction (XRD) data (up to 15.7 GPa, shown in Fig. 1) and provide complementary theoretical data based on *ab initio* calculations for comparison. The details of the total-energy study and lattice dynamics simulations, along with those of the sample preparation, are discussed in the Methods section. No evidence for a pressure-induced phase transition is observed up to 27 GPa, and we note that an apparent discontinuity in the compressibility at 8 GPa, due to the onset of non-hydrostaticity, could be misinterpreted as an indication of a second-order phase transition, or, secondly, as an indication of an atypically high bulk modulus fitted with a high order EoS, as reported in Ref. [8]. Additionally, the experimental and calculated pressure response of the YBO_3 Raman modes up to 25 GPa is also determined along with the corresponding Grüneisen parameters and pressure coefficients which were used to assign

mode symmetries to the experimental modes by comparison with the calculated modes. For the sake of completeness, the pressure behaviour of calculated infra-red active modes is also provided in the supplementary material.

2. Methods

2.1. Sample preparation

YBO_3 crystals were obtained by the flux growth method. A mixture of Y_2O_3 (99.99%, Sigma-Aldrich), B_2O_3 (99.98%, Sigma-Aldrich) and LiBO_2 (99.9+ %, Sigma-Aldrich) in a mole ratio of 1 : 1 : 17.81 was used, with LiBO_2 acting as the flux [11]. All the reagents were in the form of fine powders. A Platinum crucible with 4 cm diameter and 6 cm height was filled with the flux and the precursors, sealed with a platinum lid and put in a programmable horizontal furnace under air atmosphere. They were heated to 1150 °C at 100 °C/hour and maintained at this temperature for 10 h. Finally, the temperature of the mixture was decreased to 840 °C (−3 °C/hour) and then to room temperature (−100 °C/hour). The crucible was then removed from the furnace and promptly inverted to ease the recovery of the crystals. After the crucible had cooled down it was immersed in hot deionized water to dissolve the flux. Finally, the crystals were recovered with a paper filter and washed repeatedly with deionized water. In-house powder XRD (Cu $K\alpha$) confirmed single phase formation of the compound with no detectable impurities. Details of the subsequent synchrotron XRD

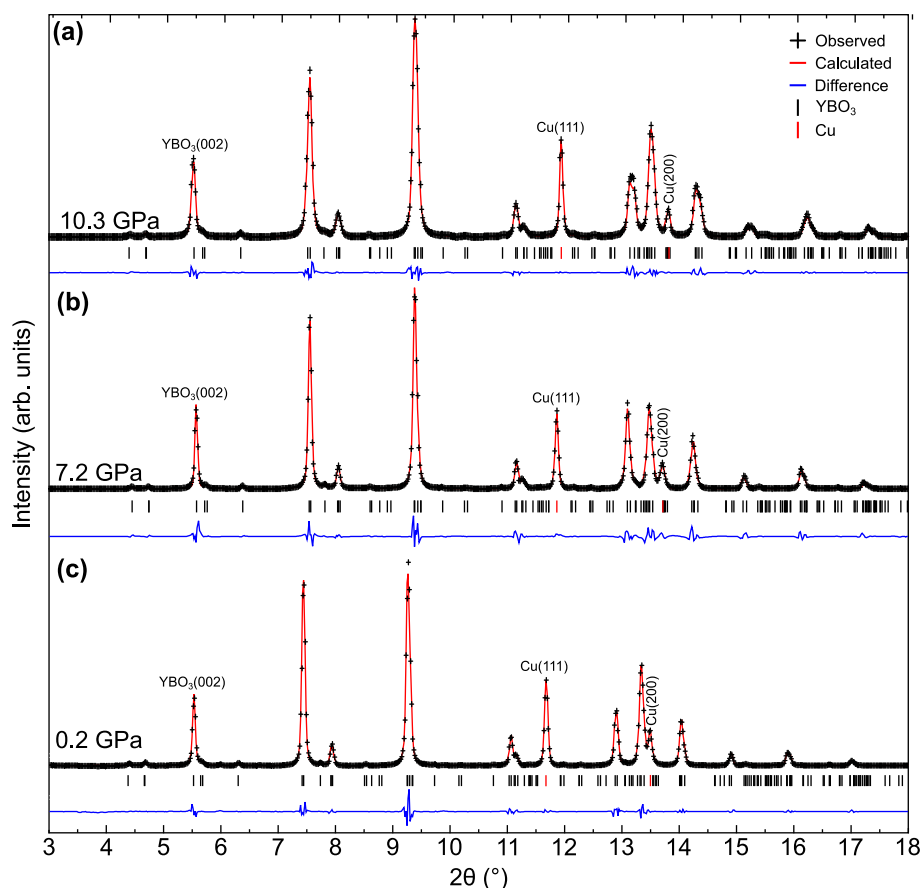


Fig. 1. High-pressure X-ray diffraction data of YBO_3 under increasing pressure. Observed experimental data are shown in black, calculated Le Bail profiles are shown in red, and the difference is shown in blue. Tick marks below the profiles indicate peak positions of YBO_3 (black) and the Cu pressure marker (red). The $\text{YBO}_3(002)$ and $\text{Cu}(111)$ reflections indicated with labels were used for the FWHM analysis in Fig. 3b. R-factors: (a) $R_p = 4.60\%$, $R_{wp} = 7.36\%$, (b) $R_p = 10.73\%$, $R_{wp} = 16.49\%$, (c) $R_p = 6.41\%$, $R_{wp} = 9.92\%$. Raw image plates are shown in Supplementary Fig. 1. (For interpretation of the references to colour in this figure legend, the reader is referred to the Web version of this article.)

experiments are provided in the next section and details of the crystal structure of the sample are provided in the X-ray crystallography section.

2.2. Measurements

For high-pressure measurements, the YBO_3 crystals were loaded into a membrane-driven diamond anvil cell (DAC) with methanol-ethanol-water pressure transmitting medium. The choice of PTM was necessary in order to test the validity of the experiments of Ref. [8] which alleged the unexpectedly large value of YBO_3 bulk modulus. Copper was used as a pressure marker in XRD measurements [12] and wide opening seats with Boehler-Almax diamonds were used to allow for data acquisition to higher scattering angles. Culet sizes were $300\ \mu\text{m}$ and tungsten gaskets were pre-indented to $30\ \mu\text{m}$ prior to loading. Angle-dispersive synchrotron powder XRD data up to $15.7\ \text{GPa}$ were collected at the BL04 beamline at ALBA Synchrotron [13] (Barcelona, Spain) using a monochromatic beam $\lambda = 0.4246\ \text{\AA}$ focused to a spot size of $20 \times 20\ \mu\text{m}$. Data were recorded on a SX165 Rayonix Mar CCD. Samples were rotated about ω over a range of $\pm 3^\circ$ with an acquisition time of $10\ \text{s}$. Powder XRD data were integrated with Dioptas [14] and Le Bail refinement of the lattice parameters was completed in JANA2006 [15]. The Rietveld analysis on the lowest pressure data (shown in Supplementary Fig. 2) was performed using SHELXT [16].

Ruby was used as a pressure marker [17] in high pressure Raman scattering (HP-RS) measurements on single-crystal samples of $30 \times 30\ \mu\text{m}$ size, $10\ \mu\text{m}$ thickness and unknown orientation. Room-temperature unpolarized HPRS measurements up to $27\ \text{GPa}$ were carried out with a Horiba Jobin Yvon LabRAM HR UV spectrometer equipped with a thermoelectrically cooled multichannel CCD detector. RS measurements with a spectral resolution better than $2\ \text{cm}^{-1}$ were performed using the $532\ \text{nm}$ line of a solid state laser with a power below $5\ \text{mW}$ in order to avoid laser heating of the sample.

2.3. Ab initio simulations

The present total-energy study of YBO_3 has been performed within the framework of density functional theory (DFT) [18]. The calculations were carried out with the VASP package [19–22] using the Y, B and O pseudopotentials provided by the VASP database. The projector augmented wave scheme (PAW) [23,24] was employed to treat ion-electron interactions taking into account the full nodal character of the all-electron charge density distribution in the core region. The basis set of plane waves was extended up to an energy cut-off of $520\ \text{eV}$, in order to achieve highly converged results and an accurate description of the electronic properties. The exchange-correlation energy was described in the generalized gradient approximation (GGA) with the PBE for solids prescription [25]. Through the minimization of the forces and the stress tensor, the monoclinic structure, space group $C2/c$ (SG no. 15), was fully relaxed to its optimized configuration at set of selected volumes. For the Brillouin Zone (BZ) integration, a dense special k -points sampling [26] of $(4 \times 4 \times 4)$ was used to have very well converged energies and forces. For sake of comparison the triclinic structure SG no. 2 was also simulated with a k -sampling of $(5 \times 4 \times 4)$. In the relaxed equilibrium configurations, the forces on the atoms were less than $0.004\ \text{eV/\AA}$ and the differences among the diagonal components of the stress tensor lower than $1\ \text{kbar}$ ($0.1\ \text{GPa}$). The resulting set of energy and volume data was fitted with a Birch-Murnaghan equation of state (EOS) [27] to evaluate the bulk modulus and its pressure derivatives. At the same time as the total energy, $E(V)$, the theoretical pressure, $P(V)$, was obtained from the calculated stress [28], like other derivatives of the energy.

The lattice dynamic study was done at the zone centre (Γ -point) of the BZ with the small-displacement method [29] which has been shown to properly work to study phonons under compression [30]. The calculations were performed at several pressures provided the frequency and symmetry of the phonon modes and allow to identify the symmetry and eigenvectors of the Raman and infrared modes.

3. Results

3.1. X-ray crystallography

At ambient temperature YBO_3 crystallises into a pseudo-vaterite structure, determined unambiguously via neutron diffraction [31], which is crucial for the photoluminescent properties of YBO_3 . It is characterised by a monoclinic unit cell (space group $C2/c$ (no. 15)) in which BO_4 -tetrahedra form three membered B_3O_9 -rings (shown in Fig. 2). The B_3O_9 -rings fragment into individual trigonal-planar BO_3 -units upon heating to approximately $1000\ ^\circ\text{C}$ and the structure maintains the same $C2/c$ space symmetry [31,32]. Previous high pressure studies of YBO_3 doped with Eu^{3+} ions have not observed any pressure induced phase transitions, either in photoluminescence [7] or synchrotron XRD measurements [8], up to at least $41\ \text{GPa}$.

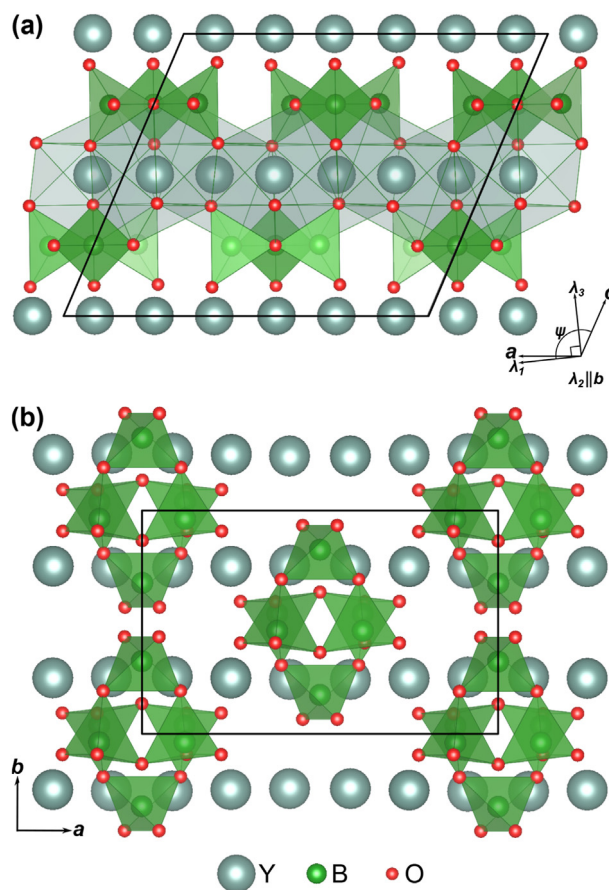


Fig. 2. The YBO_3 crystal structure. (a): Unit cell viewed along the b -axis to emphasise the alternating layers of Y-atoms and B_3O_9 -rings. BO_4 -tetrahedra are shown in green. The YO_8 -dodecahedra, shown in grey, are included for the middle plane of Y-atoms only. The compass displays the experimentally determined principal axes of compressibility (λ_1 and λ_3) in addition to the crystallographic axes (a and c). (b): Unit cell viewed along the c -axis. The reader is referred to Refs. [31] for a complete YBO_3 structure solution. (For interpretation of the references to colour in this figure legend, the reader is referred to the Web version of this article.)

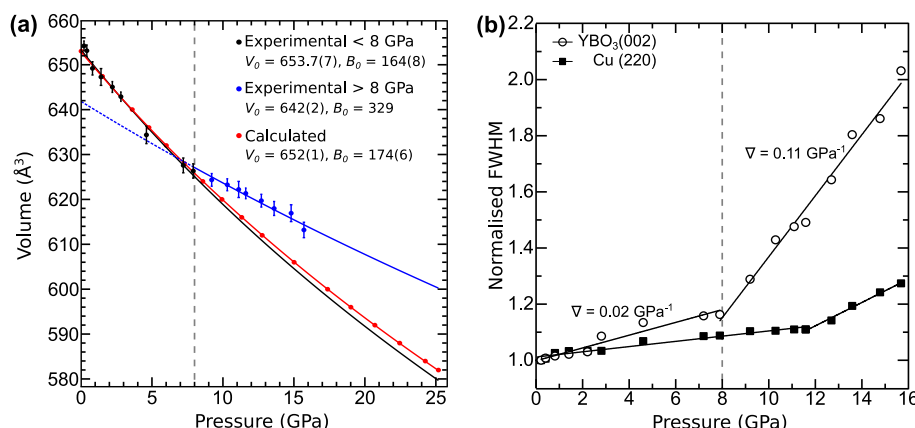


Fig. 3. Variation of YBO_3 unit cell volume and X-ray diffraction peak width with pressure. (a) Lines correspond to second-order ($B'_0 = 4$) Birch-Murnaghan equations of state. Experimental data below (above) 8 GPa are shown in black (blue) and calculated data are shown in red. (b) Normalised FWHM for Gaussian functions fitted to the $\text{YBO}_3(002)$ and $\text{Cu}(220)$ reflections labelled accordingly in Fig. 1. These reflections were selected for FWHM comparison because they exhibit no overlapping reflections. The vertical grey dotted line is located at 8 GPa in both panels. (For interpretation of the references to colour in this figure legend, the reader is referred to the Web version of this article.)

The crystal structure of YBO_3 was probed by angle-dispersive synchrotron powder XRD to 15.7 GPa at ambient temperature. The raw diffraction image plates (Supplementary Fig. 1) show diffraction rings which contain some bright spots, indicating that the sample was a coarse powder containing additional larger crystallites. In this work Le Bail refinements were sufficient to investigate the pressure-induced response of the lattice parameters and the coarse powder did not affect the analysis. A table of lattice parameters and residual discrepancy values is provided in Supplementary Table 1. Nonetheless, Rietveld analysis on the lowest pressure data allowed us to obtain the Y and O-atom positions, however, due to the relatively lower scattering cross-section it was not possible to solve the B-atom positions (see also Supplementary Table 2). The Rietveld refinement profile and corresponding Y and O-atom positions are provided in Supplementary Fig. 2 and Supplementary Table 2 respectively and the reader is referred to Ref. [31] for the YBO_3 structure.

Here, YBO_3 is observed to exhibit a $C2/c$ monoclinic structure from ambient pressure up to the highest pressure studied with XRD of 15.7 GPa. At 0.2 GPa the reflections from YBO_3 were here indexed to the known monoclinic lattice with unit-cell dimensions of: $a = 11.3231(8) \text{ \AA}$, $b = 6.5608(7) \text{ \AA}$, $c = 9.5574(6) \text{ \AA}$, $\beta = 112.870(7)^\circ$ and $V = 654.2(11) \text{ \AA}^3$ where the estimated standard deviations in the least significant digit are indicated in parentheses. The space group search was constrained to C-centred symmetries based on the $C2/c$ space group determined from single crystal neutron diffraction of ref [31]. Two independent space group tests were performed: the first by Jana2006 during the Le Bail refinement, and the second by Shelxt during the estimation of the structure for Rietveld refinement. Both tests found the $C2/c$ space group to be the best C-centred symmetry. The $P6_3/m$ previously suggested (Ref. [33]) does not account for all observed reflections as shown in Supplementary Fig. 3.

The results of the Le Bail analysis are used throughout the manuscript as the basis for analysis relating to bulk modulus (section 3.2) and isothermal compressibility (section 3.3). Furthermore, the Grüneisen parameters (section 3.4) are subsequently calculated using the bulk modulus determined from the unit cell volumes of the Le Bail analysis.

3.2. Bulk modulus and the influence of non-hydrostaticity

The experimentally determined YBO_3 unit cell volume is shown as a function of pressure in Fig. 3a. The experimental data show an

apparent discontinuity in compressibility at 8 GPa, however, the XRD and RS data provide no evidence for phase transition over the full pressure range (up to 27 GPa). The apparent and misleading change in bulk modulus is due to the onset of non-hydrostaticity at 8 GPa, corresponding to the known hydrostatic limit for the pressure transmitting medium of methanol-ethanol-water [34], which can be observed by the abrupt increase in FWHM of the diffraction peaks illustrated in Fig. 3b. Because the X-ray beam passes through the sample along the direction of maximum stress, and because the diffraction patterns do not record the full range of d -spacings for a given set of hkl s, only some of the largest d -spacings of the distorted crystallites are observed. Consequently, calculating volume based on those inter-planar spacings does not yield data representative of the molar volume under hydrostatic conditions. Instead a larger volume is calculated which can be erroneously interpreted as a change in compressibility. Interestingly, the broadening effect of non-hydrostaticity is exacerbated in YBO_3 due to the anisotropic compressibility of its monoclinic structure. For comparison, the copper (fcc) pressure marker exhibits isotropic compressibility and it is clear in Fig. 3b that the change in FWHM for copper is more slight and occurs at higher pressure. To further investigate the compressibility of YBO_3 its isothermal compressibility tensor is determined in the following section.

Fitting a second-order ($B'_0 = 4$) Birch-Murnaghan (BM) EoS to the experimental data below 8 GPa gives a bulk modulus of $B_0 = 164(8) \text{ GPa}$, which is in good agreement with the predicted bulk modulus, $B_0 = 141 \text{ GPa}$, of Ref. [9]. During the fitting procedure (using EoSFit7 [35]) the ambient-pressure volume (V_0) was also left as a free parameter. Calculated cell volumes from the *ab initio* simulations are also provided in Fig. 3a which were fitted with $B_0 = 174(6) \text{ GPa}$. Below the hydrostatic limit there is close agreement between the theoretical and experimental data.

The bulk moduli of certain ternary oxides (ABO_4) have been shown [36,37] to be dominated by the compressibility of the constituent AO_m polyhedra rather than the BO_n . In particular for ABO_4 borates, this is especially true since BO_4 tetrahedra behave as the most rigid units in these compounds [37]. Therefore, the bulk modulus of an ABO_4 oxide material is proportional to the charge density inside the AO_m polyhedron, i.e. a high charge density results in a small compressibility. Formally, the bulk modulus can therefore be expressed as $B_0 = k \cdot Z_i/d^3$, where k is an empirical proportionality constant which relates the bulk modulus, B_0 (in GPa), to the ratio between the formal cationic charge, Z_i , and the average AO_8 polyhedral volume, d^3 , where d is the average A–O bond length (in \AA).

The proportionality constant, k , has been determined to be equal to 750 for ABO_4 ternary oxides in general [38] (and equal to 610 specifically for scheelite structures [36]). The pseudo-vaterite structure of YBO_3 is closely related and is similarly comprised of BO_4 tetrahedra and YO_8 polyhedra. Therefore, applying the above equation for ABO_4 ternary oxides ($k = 750$), with the charge of the Y cation ($3+$) and the average A–O bond distance at ambient conditions (2.366 Å), results in $B_0 = 169.9$ GPa, which agrees to within the errors with the value determined via the EoS method for the experimental hydrostatic data below 8 GPa, $B_0 = 164$ (8) GPa.

To demonstrate how the alleged $B_0 = 329 \pm 31$ GPa from Ref. [8] could have been erroneously determined, the bulk modulus for the experimental data above the hydrostatic limit (8 GPa) accurately fits the data when fixed at a value of $B_0 = 329$ GPa (solid blue line shown in Fig. 3a). The decision to constrain the EoS fits to second-order ($B_0 = 4$) facilitates comparison by limiting the number of fitting parameters. Additionally, a plot of normalised stress against Eulerian strain (F_E vs. f_E , see Ref. [39]) for the theoretical data and hydrostatic experimental data gave a close to zero gradient, indicating that a truncation of the BM EoS to second-order should reasonably fit the data (see Supplementary Fig. 4). A comparison of experimental data of this study and those of Ref. [8] are shown in Supplementary Fig. 5.

3.3. Isothermal compressibility tensor

The determination of the isothermal compressibility tensor of YBO_3 reveals that this compound is highly anisotropic. Notably, the principal axis of minimal compression is twice as stiff as the other two axes, thereby exacerbating the effects of non-hydrostaticity. The principal axes of compression are, for any crystal system, a unique set of orthogonal axes along which the compressibility is a linear function of pressure [40]. In structures where the crystallographic axes are orthogonal (such as the fcc copper used here as a pressure marker) the crystallographic and principal axes of compression are equivalent. For monoclinic structures such as YBO_3 (i.e. $a \neq b \neq c$, $\beta \neq 90^\circ$) the isothermal compressibility tensor can be calculated analytically given variable-pressure lattice parameter data [41]. The eigenvalues and eigenvectors of the compressibility tensor respectively describe the magnitudes and directions of the principal axes of compression. There is close agreement between the experimental and calculated values provided in Table 1.

The major and intermediate principal compression axes (λ_1 and

λ_2) are almost equal in magnitude, and both are approximately twice as large in magnitude as the minor compression axis (λ_3) which lies almost perpendicular to the ab -plane. These data are consistent with the structure shown in Fig. 2a. For example, the compressibility perpendicular to the ab -plane (i.e. approximately in the λ_3 direction) will be dominated by the short B–O bonds (~ 1.48 Å) within the BO_4 -tetrahedra. The compressibility parallel to the ab -plane will be dominated by the longer Y–O bonds (~ 2.36 Å) within the larger YO_8 -dodecahedra, thus resulting in the major and intermediate compression axes lying almost parallel to the ab -plane. The orientation of the axis of maximum compressibility lies in the ac -plane at an angle of $\psi = 119.9^\circ$ from c to a according to the value based on the experimental data. The direction of maximum compressibility is therefore almost parallel to the a -axis ($\beta = 112.9^\circ$) differing by an angle of only 7° . Consequently, since a is approximately twice as compressible as c , the β angle between them gets smaller with increasing pressure.

The compressibility of the theoretical B–O and Y–O bond distances is quite homogeneous for the different atoms, despite occupying different Wyckoff sites, and can be observed in Supplementary Fig. 7. This figure, together with the pressure dependence of the theoretical YO_8 and BO_4 polyhedral volumes (shown in Supplementary Fig. 8), demonstrates the relative stiffness of the BO_4 -tetrahedra compared to the larger YO_8 -dodecahedra.

The bulk modulus can be estimated via $\beta = 1/(\beta_{11} + \beta_{22} + \beta_{33})$, where the elements β_{ii} are the tensor coefficients given in Table 1. Thereby, the bulk modulus determined from the tensor coefficients is 179.9 GPa, which is in good agreement with the YBO_3 bulk moduli of 164 (8) GPa and 174 (6) GPa determined from second order BM EoS fitted respectively to experimental and calculated lattice parameter data (shown in Fig. 3a). Additionally, the PASCAL principal axis strain calculator [40] determines a similar bulk modulus of 161 (8) GPa from the experimental data when fitting a second order BM EoS, and the ab initio calculations of Ref. [9] predict a bulk modulus of 141 GPa. Therefore, the new experimental and complementary data of this study provide positive evidence that the alleged YBO_3 bulk modulus of 329 GPa of Ref. [8] is an overestimation by almost a factor of two, and that the YBO_3 bulk modulus conforms with the known compressibility systematics of isomorphic borates [10]. The theoretical bulk modulus estimated from the diagonal elements of the isothermal compressibility tensor (226.5 GPa) is larger than the equivalently

Table 1

Experimental and calculated isothermal compressibility data for YBO_3 . Ambient pressure unit cell parameters (x_0) and corresponding pressure derivatives (dx/dP) were determined from linear least squares fits to the hydrostatic high-pressure data (shown in Supplementary Fig. 6). Isothermal compressibility tensor coefficients, β_{ii} , their eigenvalues, λ_i , eigenvectors, $ev(\lambda_i)$, and angle of direction of maximum compressibility, ψ , were determined according to the analysis of Ref. [41]. The experimentally determined ψ and $ev(\lambda_i)$ are illustrated in Fig. 2a.

	Experimental	Theoretical
a_0 (Å), da/dP (Å GPa ⁻¹)	11.308 (8), -0.025 (1)	11.285 (5), -0.0201 (3)
b_0 (Å), db/dP (Å GPa ⁻¹)	6.560 (2), -0.0141 (5)	6.526 (3), -0.0117 (2)
c_0 (Å), dc/dP (Å GPa ⁻¹)	9.556 (6), -0.013 (1)	9.565 (3), -0.0092 (2)
β_0 (°), $d\beta/dP$ (rad GPa ⁻¹)	112.85 (1), -0.52 (8) $\times 10^{-3}$	112.747 (4), -0.311 (1) $\times 10^{-3}$
β_{11} (GPa ⁻¹)	2.01672×10^{-3}	1.65012×10^{-3}
β_{22} (GPa ⁻¹)	2.14946×10^{-3}	1.79269×10^{-3}
β_{33} (GPa ⁻¹)	1.39181×10^{-3}	0.97233×10^{-3}
β_{13} (GPa ⁻¹)	-0.43995×10^{-3}	-0.32579×10^{-3}
λ_1 (GPa ⁻¹)	2.24388×10^{-3}	1.78132×10^{-3}
λ_2 (GPa ⁻¹)	2.14946×10^{-3}	1.79269×10^{-3}
λ_3 (GPa ⁻¹)	1.16465×10^{-3}	0.84113×10^{-3}
$ev(\lambda_1)$ (GPa ⁻¹)	(0.96625, 0, -0.49891)	(0.98710, 0, -0.39751)
$ev(\lambda_2)$ (GPa ⁻¹)	(0, 1, 0)	(0, 1, 0)
$ev(\lambda_3)$ (GPa ⁻¹)	(0.49891, 0, 0.96625)	(0.39751, 0, 0.98710)
ψ (° from c to a)	119.9	113.4
$1/(\beta_{11} + \beta_{22} + \beta_{33})$ (GPa)	179.9	226.5

calculated experimental bulk modulus probably due to a slight underestimation of the individual axial compressibilities. The ambient pressure lattice parameters in Table 1 however do agree extremely closely between theory and experiment.

3.4. Raman spectra and Grüneisen parameters

The C2/c structure of YBO₃, with 6 formula units per primitive cell, exhibits 90 vibrational modes at the zone centre (Γ -point) of the Brillouin zone, according to group theory [42], the composition of which is: $\Gamma = 20A_g(R) + 22A_u(IR) + 22B_g(R) + 23B_u(IR) + A_u + 2B_u$, where modes are labelled as Raman active (R) and infrared-active (IR). The three unlabelled modes, $A_u + 2B_u$, are the acoustic modes. Therefore, a total of 42 Raman-active and 45 infra-red-active modes are allowed by group theory.

The RS spectrum of bulk YBO₃ at ambient pressure is shown in Supplementary Fig. 9 and labelled with tick marks in order to compare experimental and theoretically-predicted Raman-active modes. Our RS spectrum is dominated by a strong mode at 265 cm⁻¹ and is similar to those reported in the literature [7,32,43,44]. The frequencies are consistent with those reported for several pseudo-vaterite type borates [45], although the modes between 450 and 800 cm⁻¹ are here observed to be less intense.

Supplementary Fig. 10 shows the calculated one-phonon density of states (1-PDOS) and the partial 1-PDOS for each atom. It can be observed that low frequency modes (below 300 cm⁻¹) are dominated by the movement of Y atoms with some contribution of O atoms above 200 cm⁻¹. Mid-frequency modes (between 300 and 700 cm⁻¹) are dominated by the vibration of O atoms with some contribution of B atoms above 500 cm⁻¹. Finally, high-frequency modes (above 700 cm⁻¹) are dominated by vibrations of B and O atoms. In particular, B movements dominate the spectrum above 950 cm⁻¹.

The vibrational modes of ABO₄ compounds have been discussed in terms of the internal and external modes of the rigid BO₄-polyhedra [46,47]. Similarly, for pseudo-vaterite ABO₃ borates, they could be discussed in terms of the internal and external modes of B₃O₉-rings or in terms of the internal and external modes of BO₄-polyhedra [45,48,49] since BO₄-polyhedra constitute the rigid units of these compounds. Neither of these two possibilities is trivial. According to Refs. [49], the B₃O₉-ring must have 30 vibrational modes and this was not easy to reconcile with existing Raman and IR spectra at that time. Now, we know that there are 6 formula units of YBO₃ in the primitive cell of the monoclinic C2/c structure, so there must be 2 B₃O₉-rings per primitive unit cell. This means that, out of the 90 vibrational modes of YBO₃, there are 3 acoustic modes, and 87 optical modes. Out of the 87 optical modes, there are 60 internal modes of the 2 B₃O₉-rings (which generally correspond to the highest frequency modes) and the remaining 27 modes are external modes of the 2 B₃O₉-rings (which generally correspond to the lowest frequency modes), and mainly involve vibrations of Y atoms. A description of the different internal modes of the B₃O₉-rings is provided in Ref. [49].

A simpler way to understand the modes of the B₃O₉-ring is in terms of the four internal ν_1 , ν_2 , ν_3 and ν_4 vibrational modes of the free or isolated BO₄-tetrahedra. However, they are not so well known as those of many other tetrahedral units, like SiO₄ or PO₄ (Refs. [46,47,50]). In fact, the internal modes of free BO₄-tetrahedra were not reported in the first edition of Ref. [51] in 1986. Now, they are reported in the latest edition of 2009. The reason is that borates usually have BO₃ and BO₄-polyhedra that are interconnected, so it is not easy to know the vibrational modes of the isolated or free BO₃ and BO₄-units. Isolated BO₄-tetrahedra are known to occur in mineral sinhalite [52] (MgAlBO₄), behierite (TaBO₄) and

schiavinatoite [53] (NbBO₄). According to Ross et al. [49], the internal ν_1 , ν_2 , ν_3 and ν_4 modes of the free BO₄ ion in rare-earth borates with pseudo-vaterite-like structure are located at 854, 481, 1050, and 702 cm⁻¹. However, the latest edition of Ref. [51] reports that the internal ν_1 , ν_2 , ν_3 and ν_4 modes of the free BO₄ ion are at 880, 372, 886, and 627 cm⁻¹ on the basis of measurements of TaBO₄, NbBO₄ and MgAlBO₄ (Refs. [48,54]). We note that these last values of the ν_1 and ν_3 modes are somewhat strange, especially since the ν_3 mode is expected to show a considerably higher frequency than the ν_1 mode, as occur in similar NO₄ and PO₄ tetrahedra [51]. The values reported in Ref. [51] can be understood as an average of the values observed in a selection of borates [48,54]. Note that in TaBO₄, the three asymmetric B-O stretching Raman-active modes, ν_3 , are at 848 and 978–1004 cm⁻¹, the symmetric B-O stretching Raman-active mode, ν_1 , is around 900 cm⁻¹, the two asymmetric bending ν_4 Raman-active modes are at 568 and 700 cm⁻¹, and the two symmetric bending ν_2 Raman-active modes are at 284 and 461 cm⁻¹ (Refs. [48,54]). For the free PO₄ ion, the values of the four internal modes [51] are 938, 420, 1017, and 567 cm⁻¹. As an example, the internal modes of the PO₄ tetrahedra in SbPO₄ are at 937, 478, 1053, and 584 cm⁻¹ (Ref. [46]). Therefore, the values of the four internal modes of the free PO₄ ion almost correspond to the maximum values of the corresponding internal modes. Therefore, we propose that for the free BO₄ ion the values of the four internal ν_1 , ν_2 , ν_3 and ν_4 Raman-active modes should be around 900, 460, 1000, and 700 cm⁻¹, respectively. Consequently, the internal modes of the BO₄ unit in all borates should be around these values. In YBO₃, however, the presence of B₃O₉-rings likely perturbs the vibrations of the BO₄-units, so the values reported by Ross et al. [48,49] for pseudo-vaterite borates (854, 481, 1050, and 702 cm⁻¹) are more practical to understand the vibrational modes in YBO₃. Examples of different normal modes of vibration in YBO₃ plotted with the JICE software [55] are shown in Supplementary Figs. 11 to 22, where it can be seen that the different frequencies of the internal modes of the BO₄-units agree with those proposed by Ref. [49].

Fig. 4 shows selected RS spectra taken in YBO₃ during compression up to 27 GPa. As observed, the mode near 265 cm⁻¹ at room pressure dominates the RS spectrum along the whole pressure range and no evidence for a pressure induced phase transition is observed. Some modes close to the peak near 410 cm⁻¹ (at ambient pressure) seem to appear or be better observed when pressure goes above 10 GPa. We think that they correspond to modes of the monoclinic phase of YBO₃ that are better observed because of the separation of closed modes as pressure increases. All Raman modes harden with pressure and no crossing or anti-crossing is observed, thus supporting the observation in XRD that no phase transition occurs in YBO₃ over the studied pressure range. Regarding possible non-hydrostatic conditions in RS measurements, we have only detected them above 13 GPa, as usual for the methanol-ethanol mixture, since there is an overall broadening of all modes above this pressure, as exemplified by the low-frequency modes in Fig. 4a.

The theoretical and experimentally observed Raman-active modes are plotted together as a function of pressure in Fig. 5. For the sake of completeness, the pressure dependence of the theoretical infrared-active modes is shown in Supplementary Fig. 23. There is a rather good agreement between the experimentally observed and theoretically predicted Raman-active modes, particularly towards smaller wavenumbers; i.e. corresponding to the external modes of the BO₄-polyhedra. However, Raman-active modes between 450 and 800 cm⁻¹ are not clearly observed in our RS spectra, unlike in previous works [7,32,43,44]. Only at room pressure, weak modes are observed near 512, 575 and 680 cm⁻¹ that have not been followed at high pressure. One possible

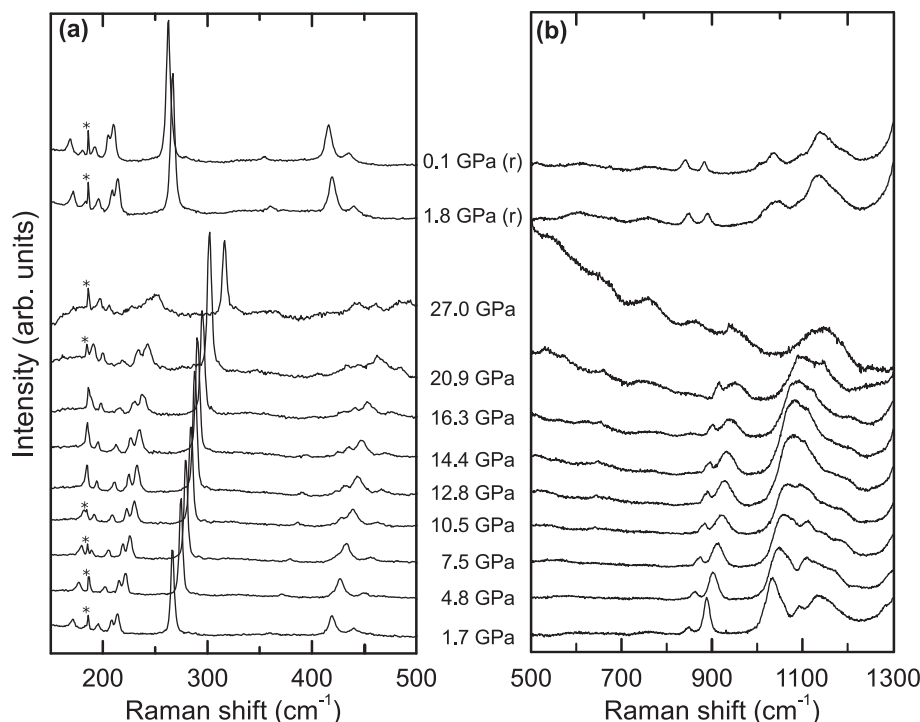


Fig. 4. Representative Raman spectra of YBO_3 on ambient temperature compression. (a) Low frequency region between 150 and 500 cm^{-1} . (b) High frequency region between 500 and 1300 cm^{-1} . Spectra acquired upon recovery to lower pressures are indicated with '(r)'. The low frequency peak indicated with an asterisk, '*', is probably an optical artefact from the experimental set-up because it does not change frequency or shape with pressure.

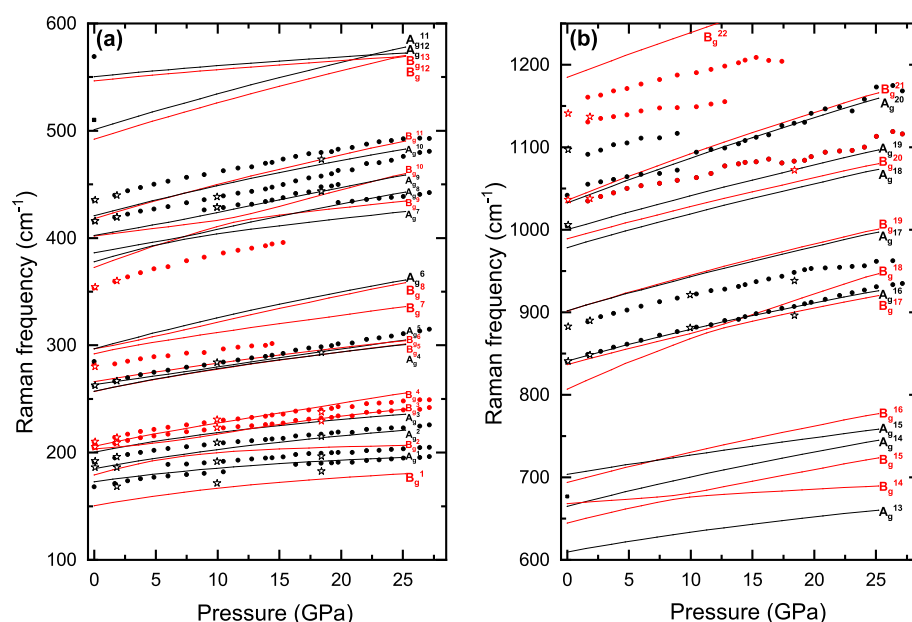


Fig. 5. Raman shift of YBO_3 as a function of pressure up to 27 GPa. (a) Low frequency region between 100 and 600 cm^{-1} . (b) High frequency region between 600 and 1250 cm^{-1} . Calculated data are shown with solid lines and are labelled with the corresponding mode symmetry. Circles (stars) correspond to experimental data obtained on (de)compression. A_g and B_g mode symmetries are shown in black and red respectively. The experimental modes were matched with calculated modes (see Table 2) based on the ambient pressure frequencies and pressure coefficients. Raman spectra are shown in Fig. 4 and Supplementary Fig. 9. (For interpretation of the references to colour in this figure legend, the reader is referred to the Web version of this article.)

explanation is that due to the single crystal orientation relative to the laser beam, the polarisation selection rules meant that the modes between 500 and 800 cm^{-1} are observed with much lower intensity than in the sample powders used in previous works on YBO_3 [32]. In fact, it must be noted that most of our assigned

experimental modes correspond to A_g .

Curiously, no Raman- or infrared-active modes are predicted to occur between 700 and 800 cm^{-1} at 0 GPa . This is a phonon gap between the stretching and bending modes of the BO_4 -unit in borates, as it occurs in TaBO_4 and NbBO_4 (Refs. [48,54]). Additionally, it

is curious that the highest frequency theoretical Raman-active mode in YBO_3 is predicted at only slightly below 1200 cm^{-1} , and that experimental Raman-active modes have been observed at frequencies above 1150 cm^{-1} . These values are much higher than the expected value for the asymmetric stretching mode of the free BO_4 -unit previously commented around 1000 cm^{-1} , so we wonder if the interconnection of BO_4 -units to form the B_3O_9 -rings leads to a hardening of the corresponding asymmetric stretching modes or even if the explanation of the Raman-active modes in YBO_3 cannot be done on the basis of the vibrations of the free BO_4 -units. In this respect, we have to note that [Supplementary Figs. 10 and 18 to 22](#); i.e. vibrations above 800 cm^{-1} shows a considerable movement of B atoms. This is not usual in stretching vibrations of other BO_4 tetrahedra, as in PO_4 . For instance, the calculated contribution of P atoms to stretching modes of the PO_4 unit in LuPO_4 is much smaller than that of O atoms [56], while in BO_4 units the contribution of B atoms is even higher than that of O atoms due to the smaller mass of B than of O (see [Supplementary Fig. 10](#)). Note also that vibrational modes of NO_4 units in Na_3NO_4 , with N mass being more similar to B than P, have asymmetric N-O stretching modes of the order of 1010 cm^{-1} (Ref. [57]), just as P-O stretching modes. Therefore, our study points to the difficulty of applying the usual vibrations of the free BO_4 ion to explain the vibrational modes in borates.

To further facilitate comparison, the ambient pressure Raman frequencies, pressure coefficients and Grüneisen parameters for the experimental modes are given in [Table 2](#) along with their corresponding theoretical modes. The assignment of theoretical modes symmetries to the experimental modes provided in [Table 2](#) was based on matching the ambient pressure frequency, ω_0 , and pressure coefficients, $\delta\omega/\delta P$, that were determined via linear fit to data in the 0–4 GPa range. The calculated zero-pressure Raman-active (infrared-active) frequencies, pressure coefficients and Grüneisen parameters are provided in [Supplementary Table 3](#) ([Supplementary Table 4](#)).

Through comparison of experimental and theoretical data, we have attributed the Raman-active mode with strongest intensity (located at 262.2 cm^{-1} at room pressure) to the A_g^5 mode (see [Supplementary Fig. 11](#)) that is a translational mode of the Y atoms.

On the other hand, the mode at 415.5 cm^{-1} at room pressure is attributed to the A_g^9 mode, related to the series of ν_2 symmetric O-B-O bending modes. The weak mode observed at 840.4 cm^{-1} at room pressure is attributed to the A_g^{16} mode, related to the series of ν_1 symmetric B-O stretching modes. Finally, the strong mode observed at 881.0 cm^{-1} at room pressure is attributed to the A_g^{17} mode, related to the series of ν_3 asymmetric B-O stretching modes. Similarly, other asymmetric B-O stretching modes occur above 1000 cm^{-1} , as already commented. An average value for the ν_3 mode in YBO_3 cannot be taken as in a free BO_4 unit since we have not measured all the asymmetric B-O stretching modes, especially that of highest frequency (expected above 1200 cm^{-1}). In any case, the value of ν_3 in YBO_3 will be clearly higher than 1000 cm^{-1} .

It must be noted that theoretically-predicted frequencies do not match well with experimental frequencies in the high-frequency region above 950 cm^{-1} (see [Fig. 5b](#)). In this context it must be recalled that calculations under the GGAPBESol prescription usually tend to underestimate the Raman-active mode frequencies by 1–5% due to a slight overestimation of the lattice parameters. These uncertainty leads to small deviations of theoretical and experimental frequencies at low frequencies, but to substantial deviations at high frequencies above 1000 cm^{-1} that can be as large as 20–60 cm^{-1} . Consequently, theoretical values of YBO_3 around 1000 cm^{-1} at 0 GPa in [Fig. 5b](#) would likely correspond to experimental frequencies of modes around 1050 cm^{-1} , while those of theoretical values close to 1050 cm^{-1} in [Fig. 5b](#) would likely correspond to experimental frequencies of modes around 1100 cm^{-1} . The only theoretical mode that seems to be overestimated is the one theoretically predicted to be close to 1180 cm^{-1} at 0 GPa that has been tentatively attributed to the mode close to 1150 cm^{-1} . The strong background in that region (see [Fig. 4](#)), where phonons seem to overlap with a photoluminescence band, has prevented us from knowing if this is the highest experimental frequency phonon or there is one at higher frequency. However, we have to note that the underestimation of the lowest frequencies and overestimation of the highest frequencies is also observed in the region between 800 and 900 cm^{-1} in [Fig. 5b](#).

Regarding the pressure coefficients of the experimentally

Table 2
Experimental and calculated ambient pressure Raman frequencies, pressure coefficients and Grüneisen parameters (γ_i) for YBO_3 . Bulk moduli (B_0) were determined from experimental data shown in [Fig. 3a](#). Pressure coefficients ($\delta\omega/\delta P$) were determined from linear fits to the data below 4 GPa in [Fig. 5](#). The relative difference between the experimental and theoretical ambient pressure mode frequencies is given by $R_\omega = 100 \times |1 - (\omega_{0,\text{exp}}/\omega_{0,\text{calc}})|$. Data for all calculated Raman and infra-red modes are provided in [Supplementary Tables 3 and 4](#) respectively.

Mode	Experimental, $B_0 = 164(8)$			Calculated, $B_0 = 174(6)$			R_ω
	$\omega_{0,\text{exp}}$	$\delta\omega/\delta P$	γ_i	$\omega_{0,\text{calc}}$	$\delta\omega/\delta P$	γ_i	
	[cm^{-1}]	[$\text{cm}^{-1}\text{ GPa}^{-1}$]		[cm^{-1}]	[$\text{cm}^{-1}\text{ GPa}^{-1}$]		
A_1^1	167.9 (3)	2.0 (1)	2.0 (1)	172.7	1.50 (6)	1.5 (1)	2.8
A_g^2	185.7 (12)	1.5 (2)	1.3 (1)	185	1.96 (6)	1.8 (1)	0.4
A_g^3	191.4 (2)	2.4 (1)	2.0 (1)	200.4	2.06 (5)	1.8 (1)	4.5
B_g^3	204.4 (2)	2.5 (1)	2.0 (1)	203.4	1.04 (7)	0.9 (1)	0.5
B_g^4	209.7 (1)	2.6 (1)	2.1 (1)	205.9	2.38 (5)	2.0 (1)	1.8
A_g^5	262.2 (2)	2.8 (1)	1.7 (1)	263.3	1.63 (1)	1.1 (1)	0.4
B_g^5	281.5 (10)	1.3 (4)	0.8 (1)	292	2.32 (11)	1.4 (2)	3.6
B_g^6	353.3 (1)	3.8 (1)	1.8 (1)	372.7	4.08 (5)	1.9 (1)	5.2
A_g^7	409.2 (4)	1.2 (2)	0.5 (1)	377.9	3.13 (6)	1.4 (1)	8.3
A_g^8	410.2 (15)	1.8 (1)	0.7 (1)	386.2	2.08 (1)	0.9 (1)	6.2
A_g^9	415.5 (3)	2.5 (1)	1.0 (1)	402.3	2.01 (1)	0.9 (1)	3.3
A_g^{10}	435.1 (4)	3.2 (1)	1.2 (1)	420.7	2.98 (6)	1.2 (1)	3.4
A_g^{16}	840.4 (5)	4.6 (2)	0.9 (2)	840.9	4.06 (6)	0.8 (1)	0.1
A_g^{17}	881.0 (16)	4.7 (6)	0.9 (1)	901.9	4.28 (11)	0.8 (2)	2.3
B_g^{20}	1027.0 (9)	4.8 (3)	0.8 (1)	989.1	4.05 (8)	0.7 (1)	3.8
A_g^{19}	1050.2 (1)	2.9 (1)	0.5 (1)	1000.3	4.19 (1)	0.7 (1)	5.0
A_g^{20}	1081.5 (11)	5.7 (4)	0.9 (1)	1032.5	5.61 (2)	0.9 (1)	4.7
B_g^{21}	1126.0 (16)	3.0 (6)	0.4 (1)	1035.9	5.79 (1)	1.0 (1)	8.7
B_g^{22}	1154.0 (20)	3.6 (7)	0.5 (1)	1184.7	5.60 (2)	0.8 (1)	2.6

observed Raman active modes of YBO_3 , it can be observed that all modes show a positive pressure coefficient and that the larger pressure coefficients correspond to the modes with larger frequencies, so in general all Grüneisen parameters are between 0.5 and 2.0 along the whole range of frequencies. This is in rather good agreement with observations from Ref. [7]. Unlike in Ref. [7], where most modes decrease in intensity with increasing pressure and are barely followed above 6 GPa, we have observed most of the modes at room pressure up to 27 GPa and their pressure dependences have been plotted in Fig. 5. Most of them showing a sublinear pressure dependence between 0 and 25 GPa, as expected over such a large pressure range [58]. It can be also mentioned that the similar sublinear pressure dependence of most vibrational modes is in agreement with the sublinear pressure dependence of the Y-O and B-O bond distances (see Supplementary Fig. 7) if we consider the general inverse relationship between frequencies and bond distances.

In summary, our HP-RS measurements confirm that YBO_3 does not undergo any pressure-induced phase transition up to 27 GPa in good agreement with XRD measurements. Moreover, our Grüneisen parameters, calculated with the experimental bulk modulus of 164 GPa, are in good agreement with those obtained by Song et al. (Ref. [7]) where the authors used the theoretical bulk modulus of 141 GPa. A brief analysis of the vibrational modes in YBO_3 has been made regarding the external and internal modes of the free BO_4 ion, which seems to show a more complex behaviour, at least in YBO_3 with B_3O_9 rings, than NO_4 and PO_4 tetrahedra. More detailed work in the regard is needed in order to better understand the lattice dynamics of borates, especially starting with those containing isolated BO_4 units, such as minerals like sinhalite, behierite and schiavinitoite.

4. Conclusion

This combined experimental-theoretical study of YBO_3 under isothermal compression up to 27 GPa has resolved the uncertainty surrounding the fundamental property of its bulk modulus and has provided a deeper study of the lattice dynamics of pseudo-vaterite borates. Variable-pressure lattice parameter data, determined from XRD experiments and *ab initio* calculations, were fitted with second order BM EoS, respectively giving YBO_3 bulk moduli of 164 (8) and 174 (6) GPa. In combination with the *ab initio* prediction of 141 GPa of Ref. [9], the claim of a YBO_3 bulk modulus of 329 GPa of Ref. [8] (almost twice as large as determined here) becomes increasingly dubious. Furthermore, the alleged bulk modulus of Ref. [8] has been recreated by intentionally fitting a second order BM EoS to non-hydrostatic variable-pressure lattice parameter data. (NB: Any BM EoS is only valid for hydrostatic data.) The discontinuity observed here in the YBO_3 compressibility around 8 GPa is due to the onset of non-hydrostaticity in the sample and no phase transitions are observed over the full pressure range either in XRD or RS experiments. The experimental and calculated pressure response of the YBO_3 Raman modes up to 27 GPa shows close agreement, therefore the corresponding frequencies and pressure coefficients were used to tentatively assign mode symmetries to the experimental modes. To further develop on the newly clarified YBO_3 bulk modulus, we obtained the isothermal compressibility tensor for YBO_3 , which, according to both theory and experiment, reveals that the principal compression axis perpendicular to the *ab*-plane is approximately twice as stiff as the two axes perpendicular to it. The highly anisotropic compressibility of YBO_3 is explained due to a combination of its monoclinic structure and the relative incompressibility of the constituent BO_4 -tetrahedra in comparison to the softer YO_8 -dodecahedra.

Data availability

All relevant data are available from the corresponding author upon reasonable request.

Author contributions

D.E. and F.J.-M. conceived and designed the project. F.J.-M., V.P.C.-G., J.Á.S., O.G. and C.P. conducted the experiments. R.T., D.E. and K.K.M. analysed the data. R.T., D.E., A.G., P.R.-H. and M.B. wrote the paper. A.G. and P.R.-H. performed the calculations. M.B. Synthesised the YBO_3 crystals.

Author information

Readers are welcome to comment on the online version of the paper. Correspondence and requests for materials should be addressed to R.T. (Robin.Turnbull@uv.es).

CRediT authorship contribution statement

Robin Turnbull: Conceptualization, Writing - original draft, Formal analysis, Visualization. **Daniel Errandonea:** Conceptualization, Writing - review & editing, Supervision, Funding acquisition, Formal analysis, Resources. **Vanesa Paula Cuenca-Gotor:** Investigation. **Juan Ángel Sans:** Writing - review & editing, Investigation. **Oscar Gomis:** Writing - review & editing, Investigation. **Alfonso Gonzalez:** Software. **Plácida Rodríguez-Hernandez:** Software. **Catalin Popescu:** Methodology, Investigation, Resources. **Marco Bettinelli:** Writing - review & editing, Methodology, Investigation. **Karuna K. Mishra:** Writing - review & editing, Investigation. **Francisco Javier Manjón:** Conceptualization, Writing - review & editing, Supervision, Funding acquisition, Formal analysis, Resources.

Declaration of competing interest

The authors declare that they have no known competing financial interests or personal relationships that could have appeared to influence the work reported in this paper.

Acknowledgements

The authors thank the financial support from the Spanish Ministerio de Ciencia, Innovación y Universidades, Spanish Research Agency (AEI), Generalitat Valenciana, and European Fund for Regional Development (ERDF, FEDER) under grants no. F152017-83295-P, MAT2016-75586-C4-1/2/3-P, RTI2018-101020-BI00, PID2019-106383 GB-C41/C42/C43, RED2018-102612-T (MALTA Consolier Team), and Prometeo/2018/123 (EFIMAT). R.T. acknowledges funding from the Spanish MINECO via the Juan de la Cierva Formación program (FJC2018-036185-I), and J.Á.S. acknowledges funding from the Ramón y Cajal fellowship program (RYC-2015-17482). The authors gratefully thank Erica Viviani (Univ. Verona) for expert technical assistance. The authors also acknowledge ALBA synchrotron (Barcelona, Spain) for provision of synchrotron radiation facilities at the MSPD-BL04 beamline. Parts of this research were carried out under proposal 2016021648.

Appendix A. Supplementary data

Supplementary data to this article can be found online at <https://doi.org/10.1016/j.jallcom.2020.156562>.

References

- [1] K. Das, A. Marathe, X. Zhang, Z. Zhao, J. Chaudhuri, Superior white light emission and color tunability of tri-doped $\text{YBO}_3:\text{Tb}^{3+}, \text{Eu}^{3+}$ and Dy^{3+} for white light emitting diodes, *RSC Adv.* 6 (97) (2016) 95055–95061, <https://doi.org/10.1039/c6ra18217h>.
- [2] X. Zhang, A. Marathe, S. Sohal, M. Holtz, M. Davis, L.J. Hope-Weeks, J. Chaudhuri, Synthesis and photoluminescence properties of hierarchical architectures of $\text{YBO}_3:\text{Eu}^{3+}$, *J. Mater. Chem.* 22 (13) (2012) 6485–6490, <https://doi.org/10.1039/C2JM30255A>.
- [3] S. Choi, B.-Y. Park, H.-K. Jung, Spherical shape with fast decaying property of solvothermally grown (Y, Gd) $\text{BO}_3:\text{Eu}^{3+}$ nanophosphor, *J. Lumin.* 131 (7) (2011) 1460–1464, <https://doi.org/10.1016/j.jlumin.2011.03.043>.
- [4] Q. Dong, Y. Wang, Z. Wang, X. Yu, B. Liu, Self-purification-dependent unique photoluminescence properties of $\text{YBO}_3:\text{Eu}^{3+}$ nanophosphors under VUV excitation, *J. Phys. Chem. C* 114 (20) (2010) 9245–9250, <https://doi.org/10.1021/jp1002287>.
- [5] G. Jia, H. You, K. Liu, Y. Zheng, N. Guo, J. Jia, H. Zhang, Highly uniform YBO_3 hierarchical architectures: facile synthesis and tunable luminescence properties, *Chem. Eur. J.* 16 (9) (2010) 2930–2937, <https://doi.org/10.1002/chem.200902834>.
- [6] Z. Wei, L. Sun, C. Liao, J. Yin, X. Jiang, C. Yan, S. Lü, Size-dependent chromaticity in $\text{YBO}_3:\text{Eu}$ nanocrystals: correlation with microstructure and site symmetry, *J. Phys. Chem. B* 106 (41) (2002) 10610–10617, <https://doi.org/10.1021/jp025967z>.
- [7] W. Song, G. Huang, R. Dai, Z. Wang, Z. Zhang, Raman scattering and photoluminescence investigation of $\text{YBO}_3:\text{Eu}^{3+}$ under high temperature and high pressure, *J. Mater. Chem. C* 3 (10) (2015) 2405–2412, <https://doi.org/10.1039/C4TC02061H>.
- [8] P. Wang, D. He, C. Xu, X. Ren, L. Lei, S. Wang, F. Peng, X. Yan, D. Liu, Q. Wang, et al., High-pressure x-ray diffraction study of $\text{YBO}_3/\text{Eu}^{3+}$, GdBO_3 , and EuBO_3 : pressure-induced amorphization in GdBO_3 , *J. Appl. Phys.* 115 (4) (2014), 043507, <https://doi.org/10.1063/1.4862653>.
- [9] D. Errandonea, A. Muñoz, J. Gonzalez-Platas, Comment on High-pressure x-ray diffraction study of $\text{YBO}_3/\text{Eu}^{3+}$, GdBO_3 , and EuBO_3 : pressure-induced amorphization in GdBO_3 , *J. Appl. Phys.* 115 (21) (2014), <https://doi.org/10.1063/1.4881057>, *J. Appl. Phys.* 115, 043507.
- [10] D. Santamaria-Perez, O. Gomis, J.A. Sans, H.M. Ortiz, A. Vegas, D. Errandonea, J. Ruiz-Fuertes, D. Martínez-García, B. García-Domene, A.L. Pereira, et al., Compressibility systematics of calcite-type borates: an experimental and theoretical structural study on ABO_3 (A = Al, Sc, Fe, and In), *J. Phys. Chem. C* 118 (8) (2014) 4354–4361, <https://doi.org/10.1021/jp4124259>.
- [11] J. Chaminade, A. García, M. Pouchard, C. Fouassier, B. Jacquier, D. Perret-Gallix, L. Gonzalez-Mestres, Crystal growth and characterization of $\text{InBO}_3:\text{Tb}^{3+}$, *J. Cryst. Growth* 99 (1–4) (1990) 799–804, [https://doi.org/10.1016/S0022-0248\(88\)80029-2](https://doi.org/10.1016/S0022-0248(88)80029-2).
- [12] A. Dewaele, P. Loubeyre, M. Mezouar, Equations of state of six metals above 94 gpa, *Phys. Rev. B* 70 (9) (2004), 094112, <https://doi.org/10.1103/PhysRevB.70.094112>.
- [13] F. Fauth, I. Peral, C. Popescu, M. Knapp, The new material science powder diffraction beamline at ALBA synchrotron, *Powder Diff.* 28 (S2) (2013) S360–S370, <https://doi.org/10.1017/S0885715613000900>.
- [14] C. Prescher, V.B. Prakapenka, DIOPTAS: a program for reduction of twodimensional X-ray diffraction data and data exploration, *High Press. Res.* 35 (3) (2015) 223–230, <https://doi.org/10.1080/08957959.2015.1059835>.
- [15] V. Petríček, M. Dušek, L. Palatinus, Crystallographic computing system JANA2006: general features, *Z. für Kristallogr. - Cryst. Mater.* 229 (5) (2014) 345–352, <https://doi.org/10.1515/zkri-2014-1737>.
- [16] G.M. Sheldrick, SHELXT—Integrated space-group and crystal-structure determination, *Acta Crystallogr. A: Foundations Adv.* 71 (1) (2015) 3–8, <https://doi.org/10.1107/S2053273314026370>.
- [17] H. Mao, J.-A. Xu, P. Bell, Calibration of the ruby pressure gauge to 800 kbar under quasi-hydrostatic conditions, *J. Geophys. Res.: Solid Earth* 91 (B5) (1986) 4673–4676, <https://doi.org/10.1029/JB091iB05p04673>.
- [18] P. Hohenberg, W. Kohn, Inhomogeneous electron gas, *Phys. Rev.* 136 (3B) (1964) B864, <https://doi.org/10.1103/PhysRev.136.B864>.
- [19] G. Kresse, J. Hafner, *Ab initio* molecular dynamics for liquid metals, *Phys. Rev. B* 47 (1) (1993) 558, <https://doi.org/10.1103/physrevb.47.558>.
- [20] G. Kresse, J. Hafner, *Ab initio* molecular-dynamics simulation of the liquid-metal–amorphous-semiconductor transition in germanium, *Phys. Rev. B* 49 (20) (1994) 14251, <https://doi.org/10.1103/physrevb.49.14251>.
- [21] G. Kresse, J. Furthmüller, Efficiency of *ab-initio* total energy calculations for metals and semiconductors using a plane-wave basis set, *Comput. Mater. Sci.* 6 (1) (1996) 15–50, [https://doi.org/10.1016/0927-0256\(96\)00008-0](https://doi.org/10.1016/0927-0256(96)00008-0).
- [22] G. Kresse, J. Furthmüller, Efficient iterative schemes for *ab initio* totalenergy calculations using a plane-wave basis set, *Phys. Rev. B* 54 (16) (1996) 11169, <https://doi.org/10.1103/PhysRevB.54.11169>.
- [23] P.E. Blöchl, Projector augmented-wave method, *Phys. Rev. B* 50 (24) (1994) 17543, <https://doi.org/10.1103/PhysRevB.50.17543>.
- [24] G. Kresse, D. Joubert, From ultrasoft pseudopotentials to the projector augmented-wave method, *Phys. Rev. B* 59 (3) (1999) 1758, <https://doi.org/10.1103/PhysRevB.59.1758>.
- [25] J.P. Perdew, A. Ruzsinszky, G.I. Csonka, O.A. Vydrov, G.E. Scuseria, L.A. Constantin, X. Zhou, K. Burke, Restoring the density-gradient expansion for exchange in solids and surfaces, *Phys. Rev. Lett.* 100 (13) (2008) 136406, <https://doi.org/10.1103/PhysRevLett.100.136406>.
- [26] H.J. Monkhorst, J.D. Pack, Special points for brillouin-zone integrations, *Phys. Rev. B* 13 (12) (1976) 5188, <https://doi.org/10.1103/PhysRevB.13.5188>.
- [27] F. Birch, Finite elastic strain of cubic crystals, *Phys. Rev.* 71 (11) (1947) 809, <https://doi.org/10.1103/PhysRev.71.809>.
- [28] O. Nielsen, R.M. Martin, Quantum-mechanical theory of stress and force, *Phys. Rev. B* 32 (6) (1985) 3780, <https://doi.org/10.1103/PhysRevB.32.3780>.
- [29] K. Parlinski, Z. Li, Y. Kawazoe, First-principles determination of the soft mode in cubic ZrO_2 , *Phys. Rev. Lett.* 78 (21) (1997) 4063, <https://doi.org/10.1103/PhysRevLett.78.4063>.
- [30] J. Ruiz-Fuertes, D. Errandonea, S. López-Moreno, J. González, O. Gomis, R. Vilaplana, F. Manjón, A. Muñoz, P. Rodríguez-Hernández, A. Friedrich, et al., High-pressure Raman spectroscopy and lattice-dynamics calculations on scintillating MgWO_4 : comparison with isomorphous compounds, *Phys. Rev. B* 83 (21) (2011) 214112, <https://doi.org/10.1103/PhysRevB.83.214112>.
- [31] J. Lin, D. Sheptyakov, Y. Wang, P. Allenspach, Structures and phase transition of vaterite-type rare earth orthoborates: a neutron diffraction study, *Chem. Mater.* 16 (12) (2004) 2418–2424, <https://doi.org/10.1021/cm0499388>.
- [32] G. Gu, D. Wang, X. Lv, S. Wan, J. You, Q. Zhang, S. Yin, In situ study on the structural transition in YBO_3 through Raman spectroscopy, *Mater. Chem. Phys.* 131 (1–2) (2011) 274–277, <https://doi.org/10.1016/j.materchemphys.2011.09.041>.
- [33] G. Chadeyron, M. El-Ghoozi, R. Mahiou, A. Arbus, J. Cousseins, Revised structure of the orthoborate YBO_3 , *J. Solid State Chem.* 128 (2) (1997) 261–266.
- [34] S. Klotz, J. Chervin, P. Munsch, G. Le Marchand, Hydrostatic limits of 11 pressure transmitting media, *J. Phys. Appl. Phys.* 42 (7) (2009), 075413, <https://doi.org/10.1088/0022-3727/42/7/075413>.
- [35] J. Gonzalez-Platas, M. Alvaro, F. Nestola, R. Angel, EosFit7-GUI: a new graphical user interface for equation of state calculations, analyses and teaching, *J. Appl. Crystallogr.* 49 (4) (2016) 1377–1382, <https://doi.org/10.1107/S1600576716008050>.
- [36] D. Errandonea, F.J. Manjon, Pressure effects on the structural and electronic properties of ABX_4 scintillating crystals, *Prog. Mater. Sci.* 53 (4) (2008) 711–773, <https://doi.org/10.1016/j.pmatsci.2008.02.001>.
- [37] J. Contreras-García, F. Izquierdo-Ruiz, M. Marqués, F. Manjón, Borates or phosphates? That is the question, *Acta Crystallogr. A: Foundations Adv.* 76 (2) (2020), <https://doi.org/10.1107/S2053273319016826>.
- [38] R.M. Hazen, L.W. Finger, J.W. Mariathasan, High-pressure crystal chemistry of scheelite-type tungstates and molybdates, *J. Phys. Chem. Solid.* 46 (2) (1985) 253–263, [https://doi.org/10.1016/00223697\(85\)90039-3](https://doi.org/10.1016/00223697(85)90039-3).
- [39] R.J. Angel, Equations of state, *Rev. Mineral. Geochem.* 41 (1) (2000) 35–59, <https://doi.org/10.2138/rmg.2000.41.2>.
- [40] M.J. Cliffe, A.L. Goodwin, PASCAL: a principal axis strain calculator for thermal expansion and compressibility determination, *J. Appl. Crystallogr.* 45 (6) (2012) 1321–1329, <https://doi.org/10.1107/S0021889812043026>.
- [41] K.S. Knight, Analytical expressions to determine the isothermal compressibility tensor and the isobaric thermal expansion tensor for monoclinic crystals: application to determine the direction of maximum compressibility in jadeite, *Phys. Chem. Miner.* 37 (8) (2010) 529–533, <https://doi.org/10.1007/s00269-009-0353-8>.
- [42] E. Kroumova, M. Aroyo, J. Perez-Mato, A. Kirov, C. Capillas, S. Ivantchev, H. Wondratschek, Bilbao crystallographic server: useful databases and tools for phase-transition studies, *Phase Transitions A Multinatl. J.* 76 (1–2) (2003) 155–170, <https://doi.org/10.1080/0141159031000076110>.
- [43] D. Boyer, G. Bertrand, R. Mahiou, A spectroscopic study of the vaterite form $\text{YBO}_3:\text{Eu}^{3+}$ processed by sol–gel technique, *J. Lumin.* 104 (4) (2003) 229–237, [https://doi.org/10.1016/S0022-2313\(03\)00077-2](https://doi.org/10.1016/S0022-2313(03)00077-2).
- [44] Y. Hao, Y. Wang, X. Hu, X. Liu, E. Liu, J. Fan, H. Miao, Q. Sun, $\text{YBO}_3:\text{Ce}^{3+}, \text{Yb}^{3+}$ based near-infrared quantum cutting phosphors: synthesis and application to solar cells, *Ceram. Int.* 42 (8) (2016) 9396–9401, <https://doi.org/10.1016/j.ceramint.2016.02.158>.
- [45] J. Denning, S. Boss, The vibrational spectra and structures of some rareearth borates, *Spectrochim. Acta Mol. Spectros* 28 (9) (1972) 1775–1785, [https://doi.org/10.1016/0584-8539\(72\)80148-X](https://doi.org/10.1016/0584-8539(72)80148-X).
- [46] A. L. d. J. Pereira, D. Santamaria-Perez, R. Vilaplana, D. Errandonea, C. Popescu, E. L. da Silva, J. A. Sans, J. RodríguezCarvajal, A. Muñoz, P. Rodríguez-Hernández, et al., Experimental and theoretical study of sbp64 under compression, *Inorg. Chem.* doi:10.1021/acs.inorgchem.9b02268.
- [47] D. Errandonea, O. Gomis, P. Rodríguez-Hernández, A. Muñoz, J. RuizFuertes, M. Gupta, S. Achary, A. Hirsch, F.-J. Manjon, L. Peters, et al., High-pressure structural and vibrational properties of monazite-type BiPO_4 , LaPO_4 , CePO_4 , and PrPO_4 , *J. Phys. Condens. Matter* 30 (6) (2018), 065401, <https://doi.org/10.1088/1361-648X/aaa20d>.
- [48] S. Ross, The vibrational spectra of some minerals containing tetrahedrally coordinated boron, *Spectrochim. Acta Mol. Spectros* 28 (8) (1972) 1555–1561, [https://doi.org/10.1016/0584-8539\(72\)80126-0](https://doi.org/10.1016/0584-8539(72)80126-0).
- [49] S. Ross, Vibrational assignments in borates with the vaterite structure, *J. Mol. Spectrosc.* 29 (1–3) (1969) 131–145, [https://doi.org/10.1016/0022-2852\(69\)90093-9](https://doi.org/10.1016/0022-2852(69)90093-9).
- [50] B. Manoun, R.T. Downs, S.K. Saxena, A high-pressure Raman spectroscopic study of hafnon, HfSiO_4 , *Am. Mineral.* 91 (11–12) (2006) 1888–1892, <https://doi.org/10.2138/am.2006.2070>.
- [51] K. Nakamoto, Infrared and Raman spectra of inorganic and coordination compounds, *Handb. Vib. Spectrosc.* (2008), <https://doi.org/10.1002/>

- 9780470405840.
- [52] D. Santamaria-Perez, D. Errandonea, O. Gomis, J. Sans, A. Pereira, F. Manjon, C. Popescu, P. Rodriguez-Hernandez, A. Munoz, Crystal structure of sinhalite MgAlBO_4 under high pressure, *J. Phys. Chem. C* 119 (12) (2015) 6777–6784, <https://doi.org/10.1021/jp512131e>.
- [53] K.-J. Range, M. Wildenauer, A.M. Heyns, Extrem kurze nichtbindende Sauerstoff-Sauerstoff-Abstände: die Kristallstrukturen von NbBO_4 , NaNb_3O_8 und NaTa_3O_8 , *Angew. Chem.* 100 (7) (1988) 973–975, <https://doi.org/10.1002/ange.19881000721>.
- [54] A. Heyns, K.-J. Range, M. Wildenauer, The vibrational spectra of NbBO_4 , TaBO_4 , NaNb_3O_8 and NaTa_3O_8 , *Spectrochim. Acta Mol. Spectros* 46 (11) (1990) 1621–1628, [https://doi.org/10.1016/0584-8539\(90\)80274-3](https://doi.org/10.1016/0584-8539(90)80274-3).
- [55] P. Canepa, R.M. Hanson, P. Ugliengo, M. Alfredsson, J-ICE: a new Jmol interface for handling and visualizing crystallographic and electronic properties, *J. Appl. Crystallogr.* 44 (1) (2011) 225–229, <https://doi.org/10.1107/S0021889810049411>.
- [56] J. Nipko, C.-K. Loong, M. Loewenhaupt, M. Braden, W. Reichardt, L. Boatner, Lattice dynamics of xenotime: the phonon dispersion relations and density of states of LuPO_4 , *Phys. Rev. B* 56 (18) (1997) 11584, <https://doi.org/10.1103/PhysRevB.56.11584>.
- [57] M. Jansen, Detection of an orthonitrate by vibrational spectroscopy: Na_3NO_4 , *Angew. Chem. Int. Ed. Engl.* 16 (8) (1977) 534–535, <https://doi.org/10.1002/ange.197705341>.
- [58] B. García-Domene, H. Ortiz, O. Gomis, J. Sans, F. Manjón, A. Muñoz, P. Rodríguez-Hernández, S. Achary, D. Errandonea, D. Martínez-García, et al., High-pressure lattice dynamical study of bulk and nanocrystalline In_2O_3 , *J. Appl. Phys.* 112 (12) (2012) 123511, <https://doi.org/10.1063/1.4769747>.